

Article

Theoretical and Experimental Investigations of Large Stokes Shift Fluorophores Based on a Quinoline Scaffold

Barbara Czaplińska¹, Katarzyna Malarz^{2,3} , Anna Mrozek-Wilczkiewicz^{2,3}, Aneta Słodek⁴, Mateusz Korzec⁴  and Robert Musiol^{1,*} 

¹ Institute of Chemistry, Faculty of Science and Technology, University of Silesia in Katowice, 75 Pułku Piechoty 1A, 41-500 Chorzów, Poland; czaplinska.basia@gmail.com

² A. Chełkowski Institute of Physics, Faculty of Science and Technology, University of Silesia in Katowice, 75 Pułku Piechoty 1, 41-500 Chorzów, Poland; katarzyna.malarz@us.edu.pl (K.M.); anna.mrozek-wilczkiewicz@us.edu.pl (A.M.-W.)

³ Silesian Center for Education and Interdisciplinary Research, University of Silesia in Katowice, 75 Pułku Piechoty 1A, 41-500 Chorzów, Poland

⁴ Institute of Chemistry, Faculty of Science and Technology, University of Silesia in Katowice, Szkolna 9, 40-007 Katowice, Poland; aneta.slodek@us.edu.pl (A.S.); mateusz.korzec@us.edu.pl (M.K.)

* Correspondence: robert.musiol@us.edu.pl

Academic Editor: Pascale Moreau

Received: 7 May 2020; Accepted: 21 May 2020; Published: 27 May 2020



Abstract: A series of novel styrylquinolines with the benzylidene imine moiety were synthesized and spectroscopically characterized for their applicability in cellular staining. The spectroscopic study revealed absorption in the ultraviolet–visible region (360–380 nm) and emission that covered the blue–green range of the light (above 500 nm). The fluorescence quantum yields were also determined, which amounted to 0.079 in the best-case scenario. The structural features that are behind these values are also discussed. An analysis of the spectroscopic properties and the theoretical calculations indicated the charge-transfer character of an emission, which was additionally evaluated using the Lippert–Mataga equation. Changes in geometry in the ground and excited states, which had a significant influence on the emission process, are also discussed. Additionally, the capability of the newly synthesized compounds for cellular staining was also investigated. These small molecules could effectively penetrate through the cellular membrane. Analyses of the images that were obtained with several of the tested styrylquinolines indicated their accumulation in organelles such as the mitochondria and the endoplasmic reticulum.

Keywords: green fluorophores; quinoline; large Stokes shift; intramolecular charge transfer; cell imaging; DFT calculations

1. Introduction

Quinoline is an attractive scaffold for designing new fluorescent agents due to its small molecular size; the presence of nitrogen, which creates good coordination properties; its ability to form hydrogen bonds, and a fair synthetic availability [1]. At the same time, quinoline itself is also known as a fluorophore unit, which further increases its potential. It is also widely used as a core molecular fragment in a broad range of drugs and biologically active substances [2–4]. For this reason, it has been claimed to be a privileged structure [5]. Our research group is interested in synthesizing and investigating quinoline derivatives [6–8]. In recent years, we obtained a series of new styrylquinolines with anticancer and antifungal properties [9,10]. Besides active compounds, some of the newly synthesized structures also turned out to be good fluorophores [11], which is in agreement with many

reports concerning the application of quinoline's structure in biological imaging. Due to their planar and rigid aromatic structure, quinolines interact with proteins and nucleic acids. Therefore, they were used for DNA and RNA imaging with good results (Figure 1A) [12–15]. Both activities (therapeutic and diagnostic) of a styrylquinoline derivative were also exploited by Staderini et al. to stain the A β amyloid plaques in Alzheimer's disease (Figure 1B) [16]. Highly fluorescent quinolines can also detect both gram-positive and gram-negative bacteria (Figure 1C) [17]. Quinoline derivatives, especially 8-hydroxy substituted are particularly good chelators for metal ions, and therefore, this type of probes have dominated this field of chemosensing [18]. Among them are the Zn²⁺ sensors, which have very good properties (Figure 1D–I) [19–22]. Indeed, the first and most commonly known fluorescent zinc ion indicator was 8-hydroxyquinoline, which was used in 1968, for detection in human plasma [23].

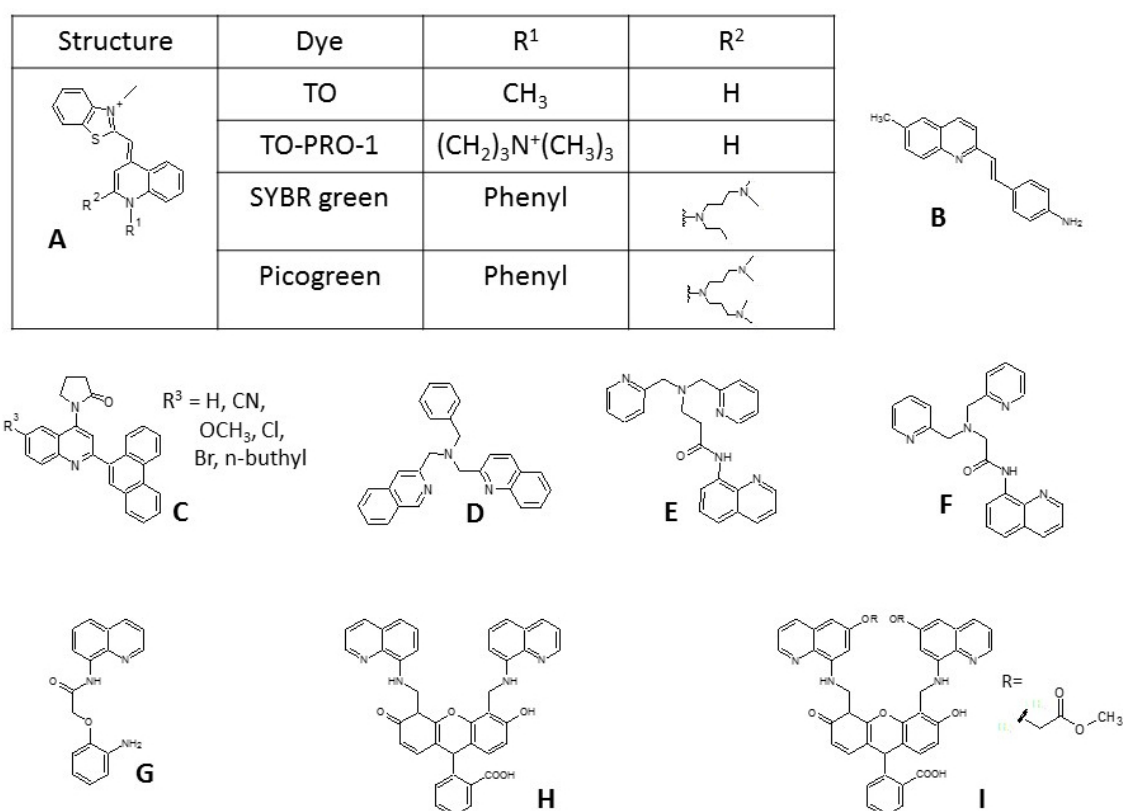


Figure 1. Examples of quinoline-based fluorophores and sensors. (A) carbocyanine dyes for DNA and RNA; (B) styrylquinoline for amyloid plaques; (C) quinoline dyes for bacterial application; (D) bisquinoline dye for metal detection; (E) and (F) dipicolylamine derivatives of quinoline as chemosensing dyes; (G) 8-aminoquinoline dye for physiological fluorescent labeling of Zn²⁺; (H) and (I) fluorescein based probes for Zn²⁺ detection.

Another appealing feature of the quinoline-related compounds is their tendency to have an intramolecular charge transfer characteristic (ICT) [24,25]. A plausible reason for this is the electron-accepting nature of the moiety because of a well-defined dipole moment. Compounds with ICT exhibit different properties in the ground and excited states, which is caused by an electronic redistribution after photoexcitation. This transient alternation leads to large changes in dipole moments and to the relaxation of the structure. The energy difference between the Frank–Condon state and the ICT state is the reason for the large Stokes shift, which is preferred in most fluorescence methods [26].

In biological applications, particularly fluorescent microscopy, the large Stokes shift which is usually over 80 nm are particularly useful for the reduction of chromatic aberrance and increase of resolution [27]. Stimulated emission depletion (STED) microscopy is a technique that utilizes res-shifted light pulse for reducing the excitation of the molecules peripheral to the excitation spot [28].

Consequently, their excitation is reduced, which allows us to overcome the diffraction barrier in high resolution images. An excellent review on large stokes shift dyes in such STED microscopy was published recently [29].

Another application of large stokes shift dyes is the Förster resonance energy transfer (FRET) microscopy, a technique based on pair dyes that can undergo direct excitation of an acceptor by the adjacent donor molecules [30]. An effective dye pair needs overlapping in the emission and excitation spectra of donor and acceptor molecule, respectively, which inevitably leads to cross-excitation of the acceptor upon the donor, resulting in false-positive results. Large stokes shift dyes are helpful to overcome this problem, increasing the threshold of detection. Moreover, compounds of this type have attracted much attention because of their possible applications in photoelectronic devices, as non-linear materials, emitters, or in organic light-emitting diodes (OLED) [31–33]. Since the ICT state emission is usually strongly dependent on environmental parameters like the solvent polarity or viscosity, push–pull compounds are also widely used as chemical sensors [34,35]. Based on our experience with the styrylquinoline compounds, we decided to substitute this scaffold with a Schiff base moiety (Figure 2).

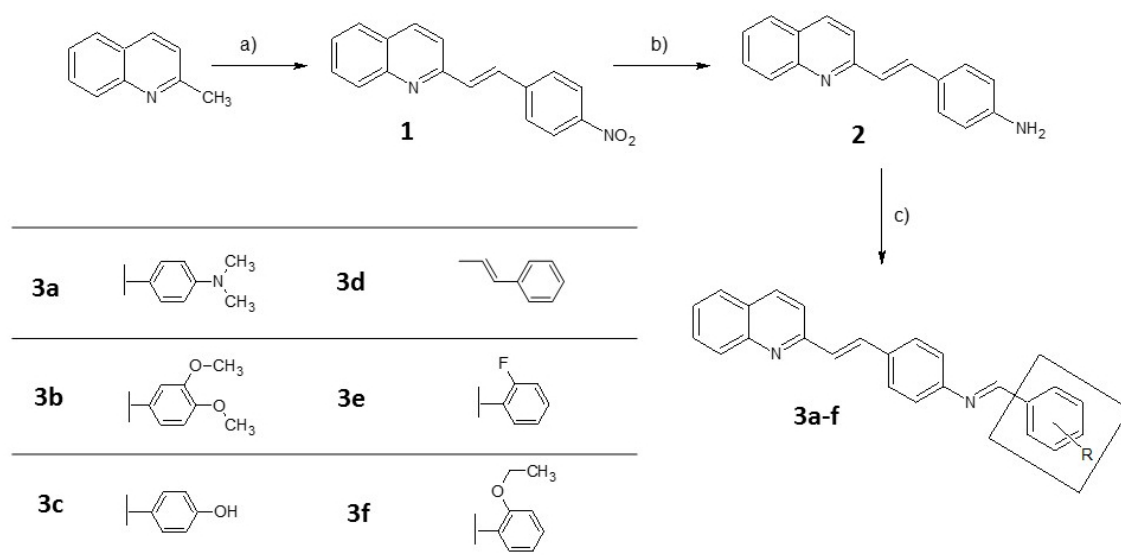


Figure 2. The synthetic pathway of compounds 3a–f. Reagents and conditions: (a) Aromatic aldehyde/ Ac_2O , (b) $\text{SnCl}_2/\text{EtOH}$, and (c) aromatic aldehyde/ EtOH .

Schiff bases are frequently reported for their antifungal, antibacterial, antiproliferative, anti-inflammatory, antimalarial, and antiviral activity [36–38]. They are also used as metal ions or pH sensors [39,40]. On the other hand, Schiff bases are relatively rarely exploited for their fluorescent potential. However, the unique properties of the imine bond, namely its polarized electron density and propensity to form a tautomeric structure, make it useful for designing compounds with ICT characteristics. Thus, in the present report, we provide the chemical, physicochemical, and optical profiles of the newly obtained compounds, together with the theoretical data and biological assays.

2. Results and Discussion

2.1. Spectroscopic Properties

2.1.1. Absorption Properties

The absorption and fluorescence of all newly synthesized compounds were investigated using UV–VIS spectroscopy. When selecting the solvents for the experiments, various properties were taken into account, such as polarity and the ability to create hydrogen bonds, since these might influence

fluorescence. The results that were obtained in this study are presented in Table 1. The obtained compounds exhibited a good excitation/emission profile. All absorption spectra consisted of two bands and the maxima of the more red-shifted ones were over 360 nm, which is desirable in cell imaging. Wavelengths shorter than 350 nm carry enough energy to destroy the complex protein structure, which interferes with the observation process and, therefore, are unsuitable for long-term experiments [41]. Absorption wavelengths above 360 nm enable avoidance of any autofluorescence from naturally occurring molecules whose excitation profile embrace higher-energy wavelengths, such as 270 nm (tyrosine) [42], 280 nm (tryptophan) [43], or 340 nm (NAD(P)H) [44]. When the absorption spectra (Figure 3) were analyzed, a relationship between a structure and the band shift were observed. The biggest red shift was recorded for compound **3a**, which had a strong electron-donating group in its structure ($N(CH_3)_2$). Therefore, attaching an electron-donating $N(CH_3)_2$ substituent in **3a** led to a markedly enhanced extinction coefficient of the low energy band, similar to the compound **3c** bearing the OH group (Table 1). Then, the spectra maxima shifted toward the longer wavelengths, together with an increase of the donating power of the substituent that was attached to a phenyl moiety (**3a** > **3c** > **3b** > **3f** > **3e**). Apparently, compound **3d** did not fit into a relationship that could be explained on a structural basis. The phenyl vinyl substituent constituted a larger conjugated aromatic system that diluted the partitive effects and changed the overall dipole of a molecule.

Table 1. Fluorescent and absorption properties of the Schiff bases **3a–f** in ethanol.

Compound	Absorption	Emission		Stokes Shift nm/cm ⁻¹
	λ_{max}/nm ($\epsilon/10^3 M^{-1} cm^{-1}$)	λ_{max}/nm	ϕ	
3a	388 (51.1) 336 (33.3)	519	0.041	131/6505
3b	368 (44.4) 276 (46.8)	512	0.054	144/7642
3c	370 (52.3) 272 (139.6)	514	0.052	144/7571
3d	372 (46.1) 274 (131.3)	512	0.034	140/7350
3e	362 (24.3) 270 (35.6)	514	0.058	152/8169
3f	366 (33.3) 272 (23.4)	514	0.079	148/7867

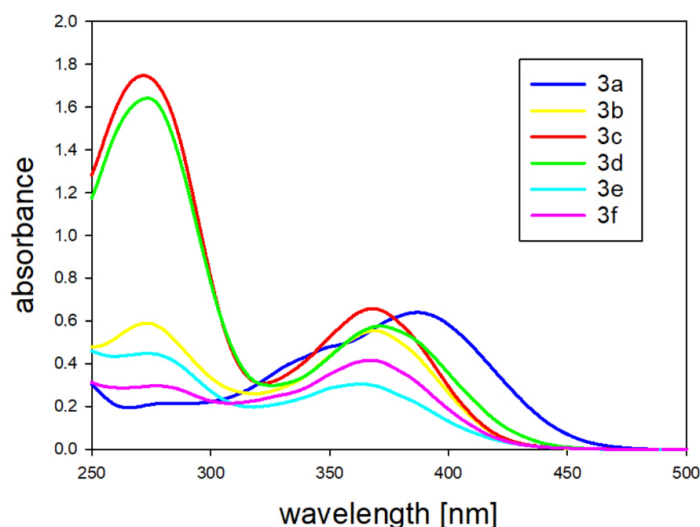


Figure 3. UV-Vis absorption spectra of the Schiff bases **3a–f** in ethanol (1.25×10^{-5} M).

2.1.2. Fluorescence Properties

The fluorescence spectra were recorded in various solvents as well, which enabled the charge transfer character of the emission to be revealed. All fluorescence spectra are presented in Figure 4 and the corresponding data are listed in Table 2. As one can see, the compounds exhibited the best fluorescent properties in ethanol. The emission peaks occurred around 514 nm in ethanol for all **3a–f** compounds, and were intense and strongly red-shifted compared to those in the chloroform and acetonitrile and were comparable to those in DMSO (except for **3a**). On the other hand, in DMSO and acetonitrile, the intensity of the emission drastically decreased in most cases, while in the chloroform, an average intensity and blue-shifted spectra could be observed.

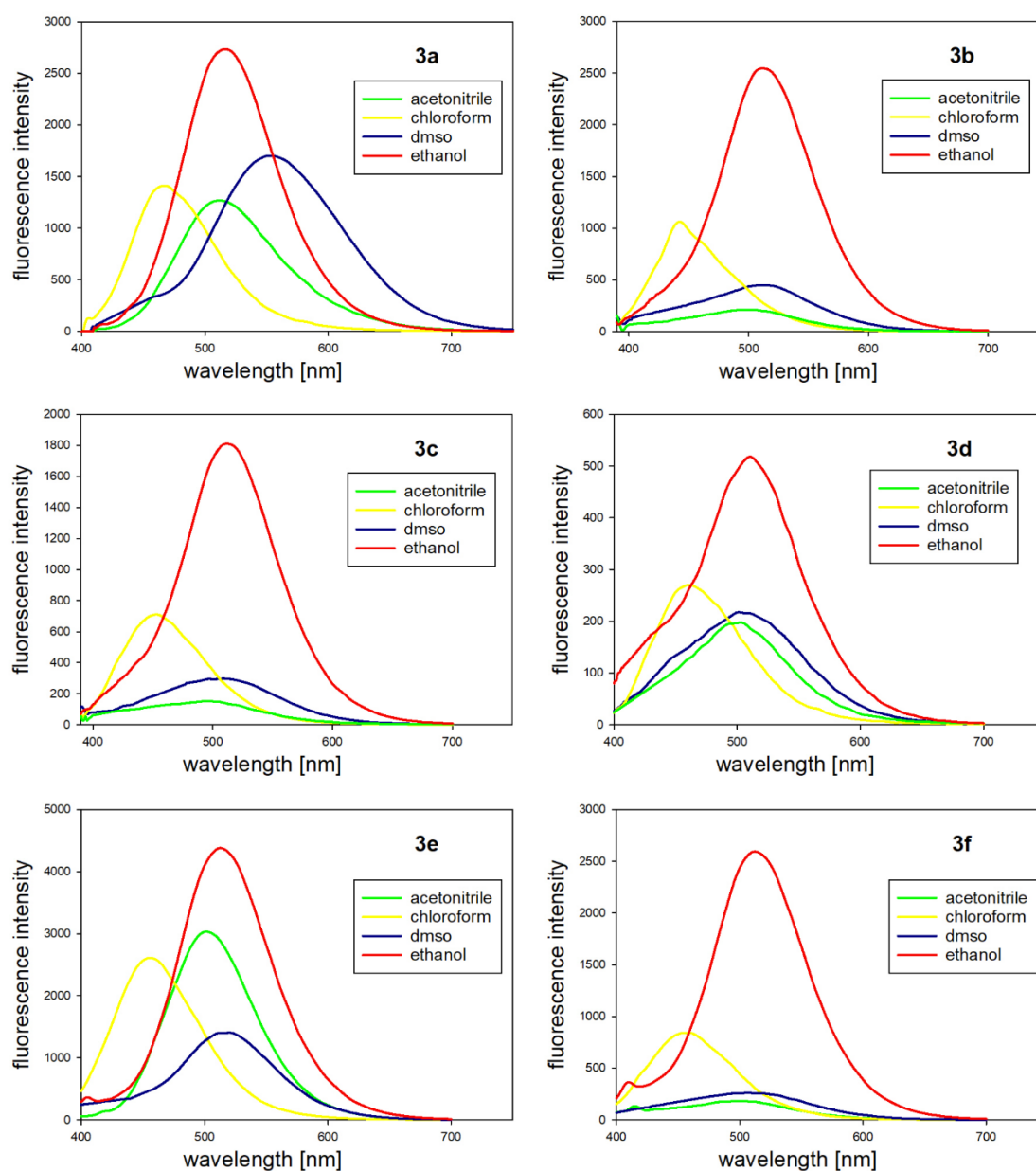


Figure 4. Fluorescence spectra of compounds **3a–f** in the various solvents (1.25×10^{-5} M).

These data suggest that the emission spectra are strongly dependent on the solvent polarity, which probably arises from a big difference in the dipole moment between the ground and excited states [45]. At the same time, it is easily noticeable that the changes had a specific tendency, which

is called positive solvatochromism—an increase of the solvent polarity induces the red shift of an emission band. The intramolecular charge transfer phenomenon is another reason for the very large Stokes shift that was observed in the synthesized compounds. The changes of the dipole moment that occurred in the excited state caused the relaxation of the solvent around an excited molecule, to obtain a state of minimum energy [46].

Table 2. Solvatochromic properties of the compounds **3a–f**; S—Stokes shift.

Compound	Chloroform			Acetonitrile			DMSO			Ethanol		
	λ_{abs} nm	λ_{em} nm	S nm/cm ⁻¹									
3a	386	467	81/4493	387	513	126/6346	400	557	157/7046	388	519	131/6505
3b	370	450	80/4804	370	500	130/7027	374	511	137/7168	368	512	144/7642
3c	368	454	86/5147	367	502	135/7327	374	510	136/7130	370	514	144/7571
3d	374	458	84/4904	372	500	128/6881	382	512	130/6646	372	512	140/7350
3e	362	456	94/5694	364	501	137/7512	370	516	146/7647	362	514	152/8169
3f	370	459	89/5240	368	500	132/7174	374	507	133/7014	366	514	148/7867

The smallest Stokes shift of 131 nm (6505 cm⁻¹) was observed for **3a** and the largest one was 152 nm (8169 cm⁻¹) for **3e**, for the measurements that were performed in ethanol. The Stokes shift is critical to the sensitivity of the fluorescence method because it enables a good detection of photons against a low background as well as the separation from an excitation source. Unfortunately, such large Stokes shifts are usually associated with small fluorescence quantum yields. These were also measured for all compounds, as presented in Table 1. The smallest quantum yield was observed for **3d** and amounted to 0.034. Whereas, for **3f**, the value was 0.079, which was the highest fluorescence efficiency that was observed. Nevertheless, all of these features together made these compounds suitable for in vitro biological imaging.

2.1.3. Influence of Water on the Spectroscopic Properties

Additionally, we decided to conduct an in-depth investigation of the spectroscopic properties of the dyes in a water environment, as is typical in analytical conditions that include the cell interior. For this purpose, because of the low water solubility of our compounds, we carried out a series of measurements in ethanol, with an increasing amount of water. The sets of the relationships that were obtained through these experiments are presented in Table 3.

Table 3. Spectroscopic properties of **3a–f** depending on the amount of water in a solution. S—BioTek Stokes shift.

Compound	Ethanol			Ethanol + Water (80%/20%)			Ethanol + Water (50%/50%)			Ethanol + Water (40%/60%)		
	λ_{abs} nm	λ_{em} nm	S nm/cm ⁻¹									
3a	388	519	131/6505	388	527	139/6797	388	534	146/7046	354	540	186/9730
3b	368	512	144/7642	368	524	156/8090	368	530	162/8305	366	534	168/8595
3c	366	514	146/7867	366	524	158/8238	366	530	164/8454	366	534	168/8595
3d	372	512	140/7350	372	524	152/7797	372	532	160/8084	366	536	170/8665
3e	362	514	152/8169	360	525	165/8730	362	529	167/8720	360	533	173/9016
3f	366	514	148/7867	366	522	156/8165	366	530	164/8454	362	534	172/8897

According to the results, water had almost no influence on the absorption spectra. The absorbance maxima of each compound did not shift, compared to their maxima in ethanol. An exception was compound **3a** whose absorption maximum was significantly blue-shifted in the 40%/60% mixture, which could be an effect of the higher protonation of the dimethylamine group in the highly protic solvent [47]. Fluorescence, on the other hand, is strongly dependent on the environmental factors, because an increased amount of water shifts the emission to the longer wavelengths. At the same time, the Stokes shifts also had higher values in the aqueous solutions, e.g., 172 nm vs. 148 nm in the case

of compound **3f**, which was in accordance with the increase of fluorescence intensity. In light of these results, we decided to further study this phenomenon. Moreover, a recently published article that investigated the hydrolysis and aggregation processes of the Schiff bases was brought to our attention, which raised more doubts about the changes that occur in water. Due to the possibility that the compounds would degrade, we used the HPLC method for the samples that contained 25% water and 75% ethanol, and measured the composition of the mixtures after 5, 15, 30, and 60 min. The results of this study are presented in Figure 5.

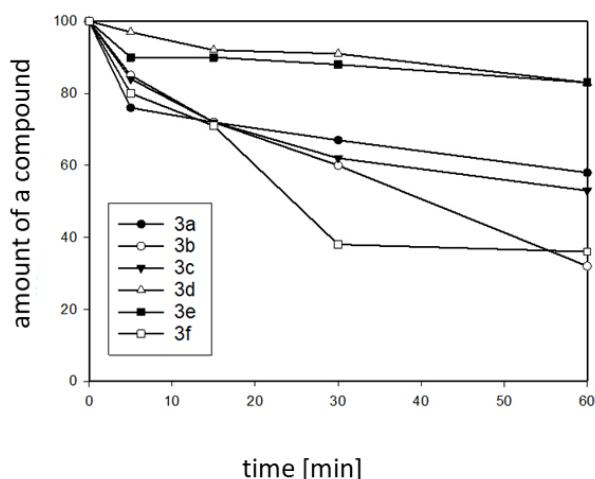


Figure 5. Plot presenting the decomposition rate of compounds **3a–f** in a water environment.

For some compounds, the decomposition was quite rapid. For compounds **3b** and **3f**, only 30–40% of the product remained after one hour. On the other hand, compounds **3d** and **3e** appeared to be rather resistant to hydrolysis. Interestingly, these observations correlated with the structural features that possibly affect the dipole moment of a molecule. The methoxy- (**3b**) and ethoxy-substituted (**3f**) compounds decomposed quickly, while the more lipophilic, less polarized ones were stable. The styryl- (**3d**) or 2-fluorophenyl- (**3e**) groups did not have an increased electron density on the imine bond, which had a positive effect on stability. It should be noted here that this type of decomposition does not always disturb the applications in water-based environments, e.g., biological systems. Recently, we published a report on the application of a pH-sensitive Schiff base, as a cellular probe for staining lysosomes [48].

2.1.4. Estimating the Dipole Moment (the Lippert–Mataga Equation)

In order to explain the large Stokes shifts in relation to changes in the structure in the excited states, we applied the Lippert–Mataga Equation (1) [49,50]. Estimating the difference between the excited- and ground-state dipole moments in this equation ($\Delta\mu = \mu_e - \mu_g$) exploited the relationship between a Stokes shift and the solvent polarity. This method is widely used in photophysical studies of the push–pull molecules to elucidate the internal charge transfer (ICT) characteristics [24,25,51,52]. The equation used was as follows:

$$\Delta\nu = \Delta E_{exc-em} = \frac{2(\mu_e - \mu_g)^2}{hca^3} \Delta f + Const. \quad (1)$$

$$\Delta f = \frac{\varepsilon - 1}{2\varepsilon + 1} - \frac{n^2 - 1}{2n^2 + 1} \quad (2)$$

where $\Delta\nu$ is the Stokes shift in a given solvent (cm^{-1}), h is the Planck's constant, c is the speed of light in a vacuum, and a is the Onsager cavity radius. The Onsager cavity radii and the

ground-state dipole moments (μ_g) were obtained from the quantum chemical calculation (Gaussian09, DFT/B3LYP/6-311+G(d)) [41,53]. The Δf is the orientation polarizability of the solvent, which measures both the electron mobility and dipole moment of a solvent molecule. Δf was calculated using Equation (2), where ϵ is the dielectric constant of the solvent and n is the optical refractive index of the solvent. Figure 6 presents the Lippert–Mataga plots, which provide the slopes to the further calculations of equation:

$$\left(\text{Slope} = \frac{2}{hca^3} (\Delta\mu_{eg})^2 \right) \quad (3)$$

whose values are presented in Table 4, together with the results that were obtained from the equation. The calculated values of $\Delta\mu_{eg}$ were 16.7 D, 18.4 D, 16.3 D, 17.8 D, 16.6 D, and 15.8 D, respectively, for compounds 3a–f. Such big differences between the dipole moments indicate the internal charge transfer (ICT) as being a process that is involved in acquiring the excited state.

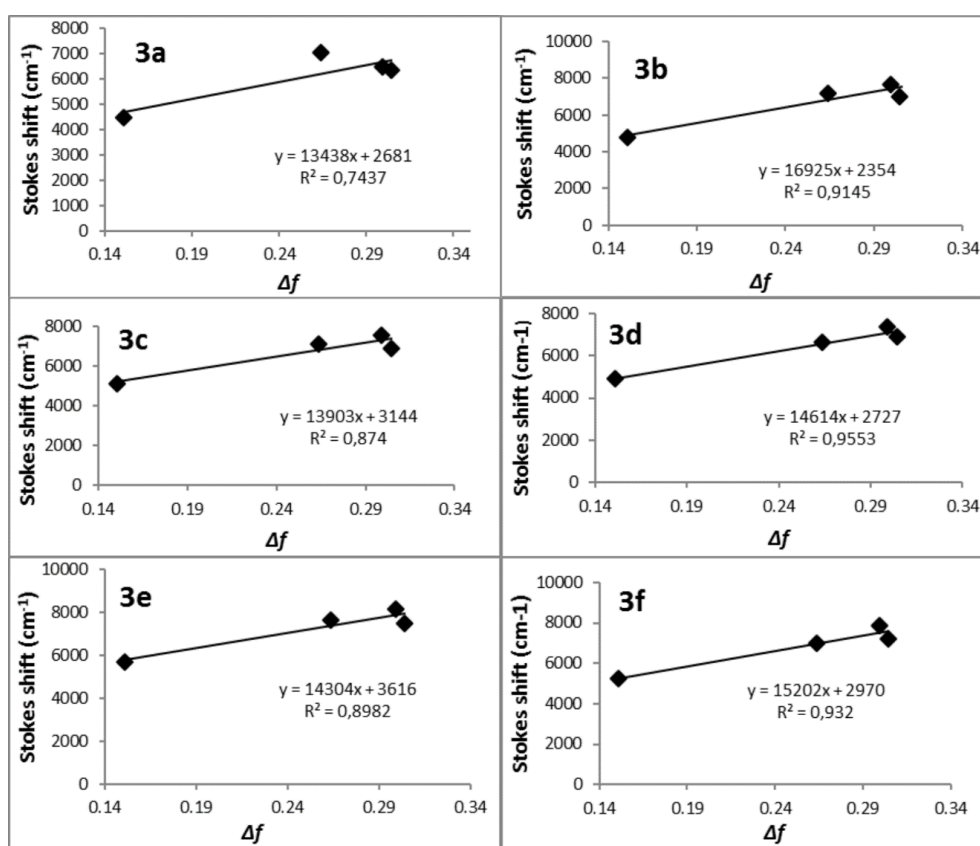


Figure 6. Plots of the Stokes shifts as a function of the solvent polarity parameter Δf (ϵ , n^2) for compounds 3a–f.

Table 4. The Onsager cavity radii, slopes, and changes of the dipole moments of compounds 3a–f.

Compound	Onsager Cavity Radius (Å)	Slope (cm ⁻¹)	$\Delta\mu_{eg}$ (Debye)	μ_g (Debye)	μ_e (Debye)
3a	5.94	13,438 ± 5578	16.7	5.6	22.3
3b	6.00	16,925 ± 3660	18.4	3.8	22.2
3c	5.48	13,903 ± 3722	16.3	3.1	19.4
3d	5.66	14,614 ± 2235	17.8	2.3	20.1
3e	5.63	14,304 ± 3404	16.6	3.2	19.3
3f	6.27	15,202 ± 2888	15.8	3.5	19.3

2.2. Theoretical Calculations

Electronic Structure and Transition Energies

To gain a more precise insight into the spectroscopic properties of the newly synthesized compounds, theoretical calculations were performed. The Time-Dependent Density Functional Theory with the CAM-B3LYP functional and the 6-311+G(d, p) basis set (TD-DFT//CAM-B3LYP//6-311+G (d, p)) appeared to be the best method for this task. Additionally, the PCM model was used to evaluate the solvent effects. The results are presented in Table 5, which includes the characteristics (oscillator strength- f , transition energy- λ /nm together with the main orbital configurations) of the main electronic transitions that were responsible for the band maxima. Furthermore, Figure 7 presents a visualization of the border orbitals HOMO and LUMO, which were involved in the main electronic transitions. The applied method gave satisfactory results compared to the experimental data. The high values of the oscillator strengths resulted from the method that was used for the calculation. According to the theoretical data, the experimental absorption maximum of the first band was mainly assigned to the $S_0 \rightarrow S_1$ transition. This transition employed the HOMOs and LUMOs, whose shapes indicated a $\pi \rightarrow \pi^*$ type of transition. In the case of compound **3a**, the electron density of the highest occupied orbital was located on the phenyl ring with the $N(\text{CH}_3)_3$ group, and the lowest unoccupied orbital embraced the quinoline structure. There was a distinct charge transfer between the donor and the acceptor units. A similar property could be observed in the case of the rest of the compounds. However, the charge transfer process was no longer distinguishable. The absorption spectra of all compounds consisted of two bands. The second bands were assigned to the higher transitions, such as $S_0 \rightarrow S_5$ or $S_0 \rightarrow S_6$, and used the HOMO orbitals with a lower energy (like HOMO-1, HOMO-3, and HOMO-6) and the LUMO orbitals with a higher energy (such as LUMO+1 and LUMO+2, and LUMO+3). Quantum calculations were also performed for the spin-allowed singlet \rightarrow singlet ($S_n \rightarrow S_0$) transitions, in order to determine the theoretical values of the fluorescence emission energy. The results are presented in Table 6. The obtained values of the emission maxima correctly reflected the experimental data.

Table 5. Electronic transition data obtained by TD-DFT//B3LYP//6-311+G (d), using a polarizable continuum model (PCM) (solvent-ethanol) for compounds **3a–f**, at the DFT-optimized geometry.

Compound	Electronic Transition	λ (nm)	f	Molecular Orbital	Percentage Contribution (%)	Experimental λ (nm)
3a	$S_0 \rightarrow S_1$	367	2.2134	HOMO \rightarrow LUMO	57	388
	$S_0 \rightarrow S_6$	274	0.0800	HOMO-1 \rightarrow LUMO+4	55	282
3b	$S_0 \rightarrow S_1$	356	1.8851	HOMO \rightarrow LUMO	86	368
	$S_0 \rightarrow S_5$	271	0.2781	HOMO-1 \rightarrow LUMO HOMO-1 \rightarrow LUMO+1	23 18	276
3c	$S_0 \rightarrow S_1$	355	1.8087	HOMO \rightarrow LUMO	88	370
	$S_0 \rightarrow S_5$	267	0.3937	HOMO-1 \rightarrow LUMO HOMO-3 \rightarrow LUMO+1	23 18	272
3d	$S_0 \rightarrow S_1$	364	2.1305	HOMO \rightarrow LUMO	85	372
	$S_0 \rightarrow S_5$	280	0.2265	HOMO-2 \rightarrow LUMO HOMO-6 \rightarrow LUMO	15 14	274
3e	$S_0 \rightarrow S_2$	354	1.6569	HOMO \rightarrow LUMO	88	362
	$S_0 \rightarrow S_5$	265	0.4493	HOMO \rightarrow LUMO+2 HOMO-1 \rightarrow LUMO	21 12	270
3f	$S_0 \rightarrow S_1$	358	1.7470	HOMO \rightarrow LUMO	87	366
	$S_0 \rightarrow S_6$	265	0.2758	HOMO \rightarrow LUMO+2 HOMO \rightarrow LUMO+3	21 11	272

Due to the structural relaxation, there was a decrease in the dihedral angle between the styrylquinoline plane and the phenyl ring (C38–N28–C27–C24, red color in Figure 8). In other words, the molecule became more planar. As a result of this change, the energy difference between the HOMO and LUMO also decreased and the energy of the emission was lower than the energy of the excitation, which resulted in a larger Stokes shift (Figure 9). These relationships were in agreement with the Jablonski diagram. The changes in the dihedral angles are presented in Table 7 and are depicted in Figure 8.

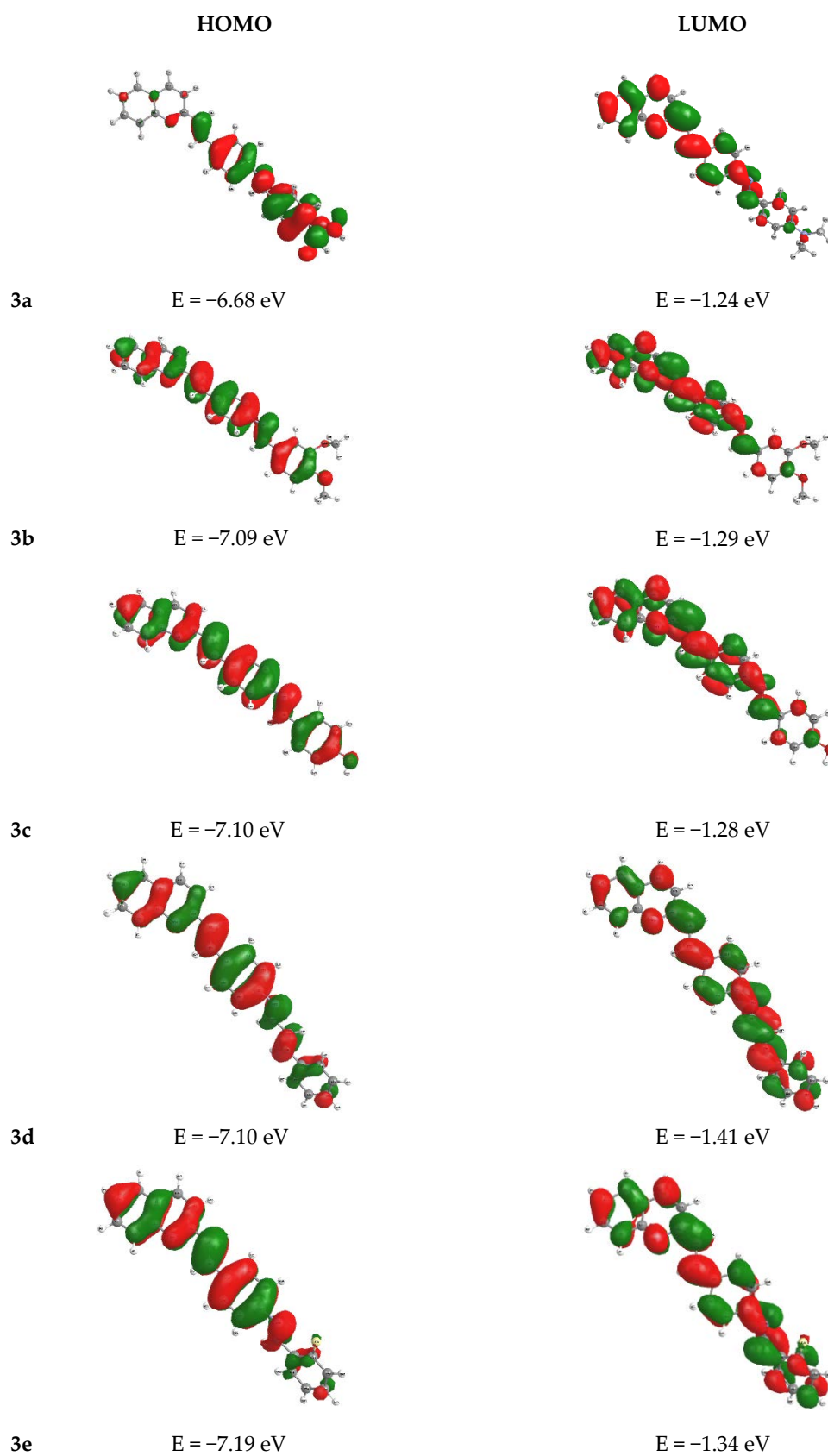


Figure 7. Cont.

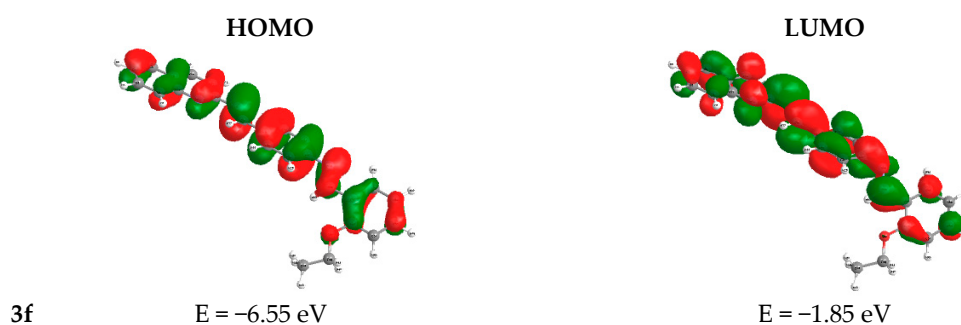


Figure 7. Visualization of the molecular orbitals that were involved in the main electronic transitions.

Table 6. Emission data obtained for **3a–f** by TD-DFT//B3LYP//6-311+G (d), using a PCM model (ethanol).

Compound	Electronic Transition	λ (nm)	f	Molecular Orbital	Percentage Contribution (%)	Experimental λ (nm)
3a	$S_0 \rightarrow S_1$	532	2.5873	HOMO \rightarrow LUMO	91	519
3b	$S_0 \rightarrow S_1$	502	2.2812	HOMO \rightarrow LUMO	93	512
3c	$S_0 \rightarrow S_1$	501	2.2154	HOMO \rightarrow LUMO	93	514
3d	$S_0 \rightarrow S_1$	540	2.4128	HOMO \rightarrow LUMO	91	512
3e	$S_0 \rightarrow S_1$	-	-	-	-	514
3f	$S_0 \rightarrow S_1$	522	1.9072	HOMO \rightarrow LUMO	91	514

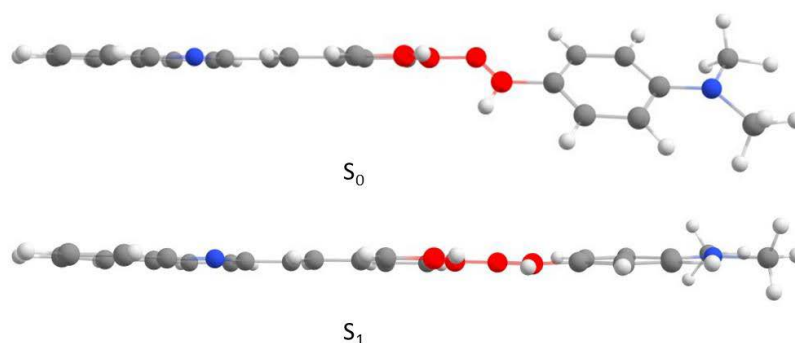


Figure 8. The geometry of compound **3a** in the ground and excited states, which was obtained by TD-DFT//B3LYP//6-311+G (d).

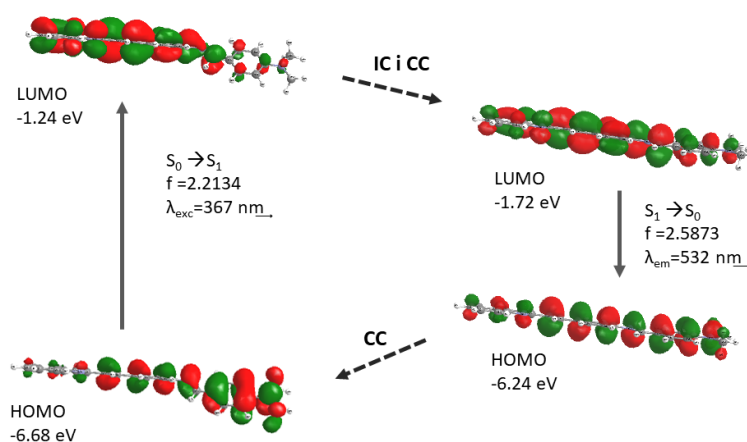


Figure 9. Geometry relaxation of compound **3a** after photoexcitation. The more planar structure was the reason for the decrease in the energy gap between the HOMO and LUMO orbitals. CC—configuration change and IC—internal conversion.

Table 7. Comparison of a compound's geometry in the ground and excited states.

Compound	Dihedral Angle (C38-N28-C27-C24)/[°]		
	Ground State S ₀	Excited State S ₁	Difference
3a	42.5	4.5	38.0
3b	42.5	15.9	26.6
3c	42.9	17.0	25.9
3d	41.7	13.3	28.4
3e	-	-	-
3f	42.7	16.0	26.7

2.3. Biological Activity and Cellular Imaging

The combination of large Stokes shifts, absorption over 350 nm, and a good fluorescent profile predestine the investigated compounds to be molecular probes for biological staining. For such applications, various physicochemical properties such as lipophilicity, protein binding, ion chelation, or halochromism could be exploited, in order to achieve specific staining effects. However, inactivity toward the biological systems is of special importance. We performed cytotoxicity tests on the human colon cancer cell line (HCT 116) and the normal human fibroblast cell line (NHDF), to evaluate the potential applications in this appealing field. The results are shown in Table 8. In general, all tested compounds had no prolonged cytotoxicity against the HCT 116 and NHDF cells, in concentrations that are useful for staining.

Incubation with synthesized compounds **3a–f** for 72 h did not affect the viability of the cells. This fact, together with their good spectroscopic properties, make them potentially useful as fluorescent dyes for biological specimens. However, with regards to the possibility of the decomposition of compounds in an aqueous environment, only two derivatives (**3e,d**) were selected for the cell imaging experiments. Additionally, for the co-localization experiments, the incubation time was reduced to 1 h, in order to minimize the risk of decomposition. The site of the accumulation of the selected compounds was examined in the HCT 116 cells, using distinct specific-organelle markers for mitochondria (MitoTracker Orange), lysosomes (LysoTracker[®] Red DND-99), and the endoplasmic reticulum (ER-Tracker[™] Red BODIPY[®] TR Glibenclamide). Apparently, these compounds tend to accumulate in the membranous structures, and their associated organelles accumulate mainly in the mitochondria and endoplasmic reticulum (ER) (Figure 10). Moreover, there is a subtle but evident relationship between the structure of a dye and the apparent site of accumulation. According to the scientific literature, it has not yet been determined why the fluorescent probes for the ER are selective. However, compounds with an affinity to the mitochondria and ER, including compounds **3d** and **3e** have a few common features, which might be crucial for their behavior in cells. Namely, these dyes usually have a medium-size aromatic system (20–30 atoms) and a moderate (or higher) lipophilicity (**3d**—logP = 7.1, **3e**—logP = 5.3). Furthermore, imines might be partially protonated in a cell, which might increase their affinity to the negatively charged mitochondrial membrane. The cationic character of a compound was also a typical feature for the ER dyes [54].

Table 8. Antiproliferative activity on the HCT 116 cell line.

Compound	Cytotoxicity-IC ₅₀ [μM]	
	HCT 116	NHDF
3a	>25	>25
3b	>25	>25
3c	>25	>25
3d	>25	>25
3e	>25	>25
3f	>25	>25

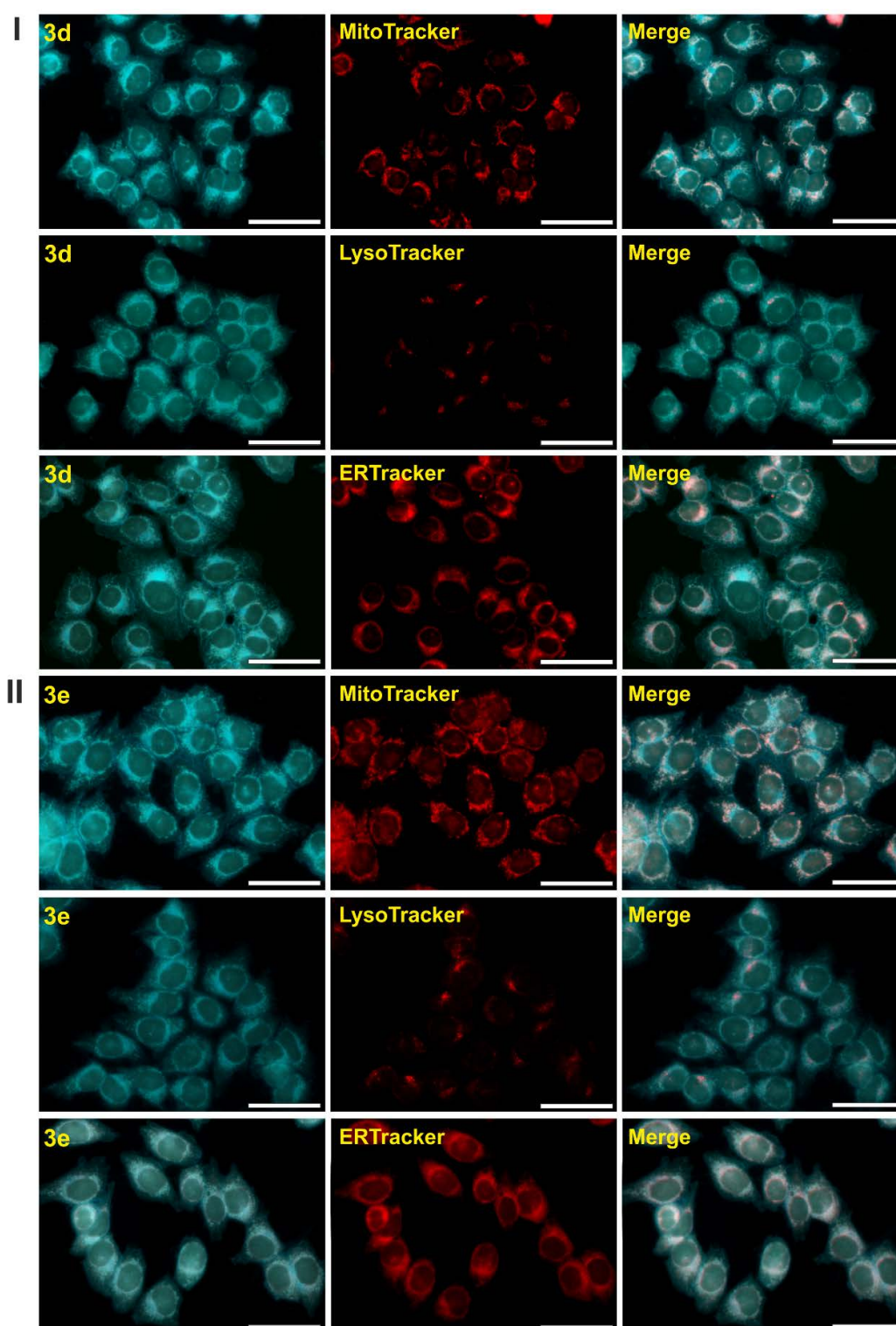


Figure 10. Fluorescence images of the HCT 116 cells that were incubated with **3d** (I) and **3e** (II) (both at a concentration of 25 μ M), for 1 h at 37 $^{\circ}$ C. The images show a co-localization with specific-organelle trackers—the mitochondria, lysosomes, and endoplasmic reticulum. The first panel represents the fluorescence of the **3d** and **3e** compounds alone, the middle panel—the specific dyes, and the last—the merged. Scale bars indicate 50 μ m. The absorption profile of the tested compounds enabled their excitation with a DAPI wavelength and the large Stokes shift helped to minimize the self-quenching effect and also boosted the signal-to-noise ratio, which in turn enabled us to obtain images of a good resolution.

3. Experimental Method

3.1. Materials and Basic Measurements

All reagents were purchased from Sigma-Aldrich. The TLC experiments were performed on aluminum-backed silica gel 40 F254 plates (Merck, Darmstadt, Germany). The plates were illuminated under UV (254 nm and 365 nm). The melting points were determined on an Optimelt MPA-100 apparatus (SRS, Stanford, CA, USA). The structures of the newly obtained compounds were confirmed by NMR spectroscopy. All NMR spectra were recorded in deuterated DMSO- d_6 as the solvent on a Bruker AM-series (Bruker BioSpin Corp., Karlsruhe, Germany). The working frequency for each compound was known. Chemical shifts were reported in ppm (δ), against the internal standard $\text{Si}(\text{CH}_3)_4$. The mass spectra were performed on a WATERS LCT Premier XE system (high-resolution mass spectrometer with a Time Of Flight (TOF) analyzer).

3.2. Synthesis and Characterization

3.2.1. Synthesis of the Starting Material

Step 1: 2-[(E)-2-(4-nitrophenyl)ethenyl]quinoline (1): The synthesis was performed according to the procedure described in [10]. The quinaldine (10 mmol) and 4-nitrobenzaldehyde (10 mmol) were mixed in acetic anhydride and heated for 20 h at 130 °C. The excess solvent was evaporated in vacuo and the obtained solid was purified using column chromatography, with dichloromethane as the eluent. The product was obtained as a bright yellow solid with a yield of 73%, and a melting point of 167 °C. ^1H NMR (400 MHz, DMSO) δ 8.41 (d, J = 8.6 Hz, 1H), 8.27 (d, J = 8.6 Hz, 2H), 8.06–7.99 (m, 4H), 7.97 (d, J = 6.4 Hz, 1H), 7.94 (d, J = 8.6 Hz, 1H), 7.78 (t, J = 7.8 Hz, 1H), 7.73 (d, J = 16.4 Hz, 1H), 7.60 (t, J = 7.4 Hz, 1H). ^{13}C NMR (126 MHz, DMSO) δ 155.27, 148.11, 147.36, 143.49, 137.24, 133.63, 132.22, 130.52, 129.30, 128.67, 128.35, 127.77, 127.17, 124.53, 120.82.

Step 2: 4-[(E)-2-(quinolin-2-yl)ethenyl]aniline (2): In a round-bottom flask, compound 1 was placed in ethanol, together with anhydrous SnCl_2 , at a molar ratio of 1:5. The mixture was heated for 2 h at a temperature of 70 °C, under nitrogen. Then, the mixture was cooled, placed in a flask with ice, and neutralized with a 5% solution of sodium bicarbonate (NaHCO_3). Next, the extraction with ethyl acetate was performed, the organic layer was washed with brine and dried over anhydrous sodium sulfate (Na_2SO_4). The product was obtained as a red solid with a yield of 61% and a melting point of 174 °C. ^1H NMR (400 MHz, DMSO) δ 8.26 (d, J = 8.6 Hz, 1H), 7.93 (d, J = 8.4 Hz, 1H), 7.89 (d, J = 8.0 Hz, 1H), 7.77 (d, J = 8.6 Hz, 1H), 7.73–7.69 (m, 1H), 7.67 (d, J = 16.1, 1H), 7.50 (t, J = 7.4 Hz, 1H), 7.42 (d, J = 8.3 Hz, 2H), 7.13 (d, J = 16.2 Hz, 1H), 6.61 (d, J = 8.3 Hz, 2H), 5.54 (s, 2H). ^{13}C NMR (126 MHz, DMSO) δ 157.03, 150.39, 148.22, 136.54, 135.54, 130.07, 129.21, 128.81, 128.18, 127.10, 125.95, 124.22, 123.28, 120.06, 114.33. ^{13}C NMR (126 MHz, DMSO) δ 157.03, 150.39, 148.22, 136.54, 135.54, 130.07, 129.21, 128.81, 128.18, 127.10, 125.95, 124.22, 123.28, 120.06, 114.33.

3.2.2. Representative Procedure for Compounds 3a–f

Compound 2 and the corresponding aldehyde were placed in a round-bottom flask, at a ratio of 1:1. Then, 5 mL of ethanol and 3 drops of acetic acid were added. The mixture was exposed to microwave irradiation for 20 min in conditions of 50 W and 83 °C. The obtained compounds were filtered and washed with ethanol. The general route for the synthesis is presented in Figure 2.

(N-[[4-(Dimethylamino)phenyl]methylidene]-4-[(E)-2-(quinolin-2-yl)ethenyl]aniline (3a): The product was obtained as a yellow solid with an yield of 62% and a melting point of 202 °C. ^1H NMR (500 MHz, DMSO) δ 8.49 (s, 1H), 8.35 (d, J = 8.6 Hz, 1H), 7.99 (d, J = 8.5 Hz, 1H), 7.95 (d, J = 7.3 Hz, 1H), 7.87 (d, J = 9.00 Hz, 1H), 7.86 (d, J = 16.5 Hz, 1H), 7.79–7.73 (m, 5H), 7.56 (t, J = 7.4 Hz, 1H), 7.46 (d, J = 16.3 Hz, 1H), 7.27 (d, J = 8.4 Hz, 2H), 6.80 (d, J = 9.0 Hz, 2H), 3.03 (s, 6H). ^{13}C NMR (126 MHz, DMSO) δ 160.31,

156.29, 153.07, 153.10, 148.24, 136.84, 134.33, 133.63, 130.88, 130.21, 129.11, 128.69, 128.22, 128.14, 127.47, 126.49, 124.40, 121.94, 120.39, 112.01. ESI-MS calcd. for $C_{26}H_{24}N_3$ 378.1970 $[M+H]^+$ found 378.1973.

N-[(3,4-Dimethoxyphenyl)methylidene]-4-[(*E*)-2-(quinolin-2-yl)ethenyl]aniline (**3b**): The product was obtained as a yellow solid with an yield of 70% and a melting point of 172 °C. 1H NMR (500 MHz, DMSO) δ 8.59 (s, 1H), 8.36 (d, $J = 8.6$ Hz, 1H), 8.00 (d, $J = 8.4$ Hz, 1H), 7.95 (d, $J = 7.5$ Hz, 1H), 7.87 (d, $J = 9.0$ Hz, 1H), 7.86 (d, $J = 16.5$ Hz, 1H), 7.80 (d, $J = 8.4$ Hz, 2H), 7.76 (t, $J = 7.7$ Hz, 1H), 7.58–7.55 (m, 2H), 7.49 (d, $J = 16.5$ Hz, 1H), 7.48 (d, $J = 8.5$ Hz, 1H), 7.32 (d, $J = 8.4$ Hz, 2H), 7.12 (d, $J = 8.4$ Hz, 1H), 3.85 (s, 6H). ^{13}C NMR (126 MHz, DMSO) δ 160.66, 156.20, 152.43, 152.37, 149.51, 148.16, 136.9, 134.22, 134.14, 130.30, 129.50, 129.10, 128.77, 128.46, 128.28, 127.46, 126.59, 124.74, 122.09, 120.45, 111.79, 109.88. ESI-MS calcd. for $C_{26}H_{23}N_2O_2$ 395.1760 $[M+H]^+$ found 395.1763.

4-(*N*-[4-[(*E*)-2-(quinolin-2-yl)ethenyl]phenyl]carboximidoyl)phenol (**3c**): The product was obtained as a yellow solid with an yield of 67% and a melting point of 248 °C. 1H NMR (500 MHz, DMSO) δ 10.17 (s, 1H), 8.54 (s, 1H), 8.36 (d, $J = 8.6$ Hz, 1H), 8.00 (d, $J = 8.4$ Hz, 1H), 7.95 (d, $J = 7.9$ Hz, 1H), 7.88 (d, $J = 8.5$ Hz, 1H), 7.86 (d, $J = 16.5$ Hz, 1H), 7.82–7.73 (m, 5H), 7.56 (t, $J = 7.5$ Hz, 1H), 7.47 (d, $J = 16.3$ Hz, 1H), 7.29 (d, $J = 8.3$ Hz, 2H), 6.90 (d, $J = 8.5$ Hz, 2H). ^{13}C NMR (126 MHz, DMSO) δ 161.26, 160.54, 156.22, 152.62, 148.16, 136.92, 134.20, 134.02, 131.30, 130.30, 129.09, 128.74, 128.33, 128.27, 127.97, 127.45, 126.57, 122.03, 120.43, 116.17. ESI-MS calcd. for $C_{24}H_{19}N_2O$ 351.1497 $[M+H]^+$ found 351.1500.

N-[(2*E*)-3-phenylprop-2-en-1-ylidene]-4-[(*E*)-2-(quinolin-2-yl)ethenyl]aniline (**3d**): The product was obtained as a yellow solid with an yield of 68% and a melting point of 195 °C. 1H NMR (400 MHz, DMSO) δ 8.49 (d, $J = 8.9$ Hz, 1H), 8.36 (d, $J = 8.6$ Hz, 1H), 8.00 (d, $J = 8.4$ Hz, 1H), 7.95 (d, $J = 8.0$ Hz, 1H), 7.89 (d, $J = 8.8$, 1H), 7.87 (d, $J = 16.8$ Hz, 1H), 7.81–7.70 (m, 5H), 7.51 (s, 1H), 7.49 (d, $J = 16.4$ Hz, 1H), 7.45–7.40 (m, 4H), 7.30 (d, $J = 8.3$ Hz, 2H), 7.20 (dd, $J = 16.0, 8.9$ Hz, 1H). ^{13}C NMR (126 MHz, CD_2Cl_2) δ 161.47, 155.89, 152.07, 148.34, 144.13, 136.21, 135.69, 134.55, 133.53, 129.63, 129.60, 129.08, 128.90, 128.66, 128.43, 128.16, 127.53, 127.36, 126.04, 121.49, 119.60. ESI-MS calcd. for $C_{26}H_{21}N_2$ 361.1705 $[M+H]^+$ found 361.1707.

N-[(2-fluorophenyl)methylidene]-4-[(*E*)-2-(quinolin-2-yl)ethenyl]aniline (**3e**): The product was obtained as a yellow solid with an yield of 68% and a melting point of 124 °C. 1H NMR (400 MHz, DMSO) δ 8.85 (s, 1H), 8.37 (d, $J = 8.6$ Hz, 1H), 8.14 (t, $J = 7.1$ Hz, 1H), 8.00 (d, $J = 8.4$ Hz, 1H), 7.96 (d, $J = 8.0$ Hz, 1H), 7.89 (d, $J = 8.8$, 1H), 7.87 (d, $J = 16.8$ Hz, 1H), 7.83 (d, $J = 8.3$ Hz, 2H), 7.76 (t, $J = 7.6$ Hz, 1H), 7.67–7.54 (m, 2H), 7.51 (d, $J = 16.3$ Hz, 1H), 7.43–7.33 (m, 4H). ^{13}C NMR (126 MHz, DMSO) δ 163.65, 161.64, 156.11, 153.80, 151.80, 148.14, 136.96, 135.09, 134.22 (d, $J = 8.4$ Hz), 133.99, 130.32, 129.01 (d, $J = 23.5$ Hz), 128.80, 128.31 (d, $J = 8.5$ Hz), 127.49, 126.64, 125.42, 123.88 (d, $J = 8.8$ Hz), 122.26, 120.46, 116.69 (d, $J = 20.6$ Hz). ESI-MS calcd. for $C_{24}H_{18}FN_2$ 353.1448 $[M+H]^+$ found 353.1452.

N-[(2-ethoxyphenyl)methylidene]-4-[(*E*)-2-(quinolin-2-yl)ethenyl]aniline (**3f**): The product was obtained as a yellow solid with an yield of 55% and a melting point of 167 °C. 1H NMR (500 MHz, DMSO) δ 8.91 (s, 1H), 8.36 (d, $J = 8.6$ Hz, 1H), 8.04 (dd, $J = 7.7, 1.8$ Hz, 1H), 8.00 (d, $J = 8.5$ Hz, 1H), 7.96 (d, $J = 8.1$ Hz, 1H), 7.89 (d, $J = 8.5$ Hz, 1H), 7.87 (d, $J = 16.5$ Hz, 1H), 7.80 (d, $J = 8.4$ Hz, 2H), 7.78–7.74 (m, 1H), 7.57 (dt, $J = 8.0, 6.9, 1.1$ Hz, 1H), 7.54–7.51 (m, 1H), 7.49 (d, $J = 16.4$ Hz, 1H), 7.29 (d, $J = 8.4$ Hz, 2H), 7.17 (d, $J = 8.2$ Hz, 1H), 7.07 (t, $J = 7.5$ Hz, 1H), 4.18 (q, $J = 7.0$ Hz, 2H), 1.40 (t, $J = 7.0$ Hz, 3H). ^{13}C NMR (126 MHz, DMSO) δ 159.23, 156.18, 156.14, 152.85, 148.20, 136.91, 134.51, 134.12, 133.75, 130.26, 129.12, 128.80, 128.65, 128.25, 127.49, 127.43, 126.58, 124.55, 121.96, 121.12, 120.44, 113.54, 64.52, 14.76. ESI-MS calcd. for $C_{26}H_{23}N_2O$ 379.1810 $[M+H]^+$ found 379.1806.

3.3. Biological Properties

3.3.1. Cell Culture

The human colon carcinoma cell line HCT 116 was obtained from ATCC. The cells were grown as monolayer cultures in 75 cm² flasks (Nunc) in Dulbecco's modified Eagle's medium with antibiotic gentamicin (200 μ L/100 mL medium). DMEM was supplemented with 12% heat-inactivated fetal

bovine serum (Sigma). The cells were cultured under standard conditions, at 37 °C in a humidified atmosphere at 5% CO₂.

3.3.2. Cytotoxicity Studies

The cells were seeded in 96-wells plates (Nunc) at a density of 5×10^3 cells/well and incubated at 37 °C for 24 h. The assay was performed, following a 72 h incubation with varying concentrations of the compounds (**3a–f**) that were being tested. Then, 20 µL of the CellTiter 96[®]AQueous One Solution-MTS (Promega) was added to each well (with 100 µL DMEM without phenol red) and incubated for 1 h at 37 °C. The optical densities of the samples were analyzed at 490 nm, using a multi-plate reader Synergy 4 (BioTek, BioTek Instruments, Winooski, VT, USA). The results were calculated as the inhibitory concentration (IC₅₀) values using the GraphPad Prism 7, and are expressed as a percentage of the control. Each individual compound was tested in triplicates in a single experiment, with each experiment being repeated three times.

3.3.3. Cellular Staining

The cells were seeded onto glass slides at a density of 3×10^5 cells/slide and were incubated at 37 °C for 24 h. Then, the medium was removed and the solutions of **3a–f**, at a concentration of 25 µM, were added. The cells were then further incubated for 1 h and 2 h, under standard conditions—at 37 °C in a humidified atmosphere at 5% CO₂. After incubation, the cells were washed three times with PBS and fixed with 3.7% paraformaldehyde, for 10 min. The cellular staining with compounds being tested was observed using a Nikon Eclipse Ni-U microscope, equipped with a Nikon Digital DS-Fi1-U3 camera and the corresponding software (Nikon, Tokyo, Japan).

3.3.4. Subcellular Localization

The cells were seeded onto glass slides at a density of 3×10^5 cells/slide and incubated at 37 °C for 24 h. Then, the medium was removed and the solutions of **3a–f**, at a concentration of 25 µM, were added. The cells were then further incubated for 1 h and 2 h. After incubation, the cells were rinsed with PBS (pH 7.2) and the staining procedures were performed according to the protocols of the providers. In brief, a serum-free medium that contained MitoTracker[®] Orange (100 nM, 30 min incubation, Molecular Probes), ER-Tracker[™] Red BODIPY[®] TR Glibenclamide (1 µM, 30 min incubation, Molecular Probes), and LysoTracker[®] Red DND-99 (500 nM, 1 h incubation, Molecular Probes) or Hoechst 33342 (6.5 µM, 15 min incubation, Molecular Probes) were added. After staining with organelle-specific trackers, the cells were washed three times with PBS and fixed with 3.7% paraformaldehyde for 10 min. The subcellular localization was observed using a Nikon Eclipse Ni-U microscope equipped with a Nikon Digital DS-Fi1-U3 camera and the corresponding software. The analysis and processing of the images were performed using an Image J 1.41 (Wayne Rasband, National Institutes of Health, Bethesda, MD, USA).

3.4. Spectroscopic Studies

The absorption and fluorescence spectra were measured at room temperature in a 10 mm quartz cell, using a U-2900 spectrophotometer (Hitachi) and an F-7000 spectrofluorometer (Hitachi), respectively. Due to the low solubility of the compounds in the applied solvents, the solutions that were used in the test of the solvatochromic behavior contained 1% of DMSO, to improve the solubility. The quantum yields of fluorescence were determined using the absolute method at room temperature, using an integrating sphere with a solvent as a blank on an FLS-980 spectrophotometer. The compounds were excited at the wavelength that corresponded with the absorption wavelength of the compounds.

3.5. Theoretical Calculations

The geometrical parameters of an investigated compound and its electronic properties in the ground and excited states were calculated within the DFT and TD-DFT approximations, using the Gaussian 09 software package [53] with the CAM-B3LYP exchange-correlation functional [55–57] and the 6-311+G (d, p) basis set. The effects of the solvent were evaluated using the polarizable continuum model (PCM) [58,59] in which a cavity was created via a series of overlapping spheres [60] with the standard dielectric constants (ϵ) of 24.55 for ethanol. The lowest 50 singlet–singlet vertical electronic excitations based on the B3LYP optimized geometries and the optimization of the first excited states were computed using the time-dependent density functional theory (TD-DFT) formalism [61]. The visualization of the molecular orbitals and analysis of the energy levels were performed using the Chemission software.

4. Conclusions

A series of styrylquinoline dyes with a Schiff base fragment was designed and synthesized, and their physicochemical parameters and spectroscopic features were determined. All compounds had a high Stokes shift and strong solvatochromism. Along with the calculations that were carried out accordingly, these suggested an intramolecular charge-transfer mechanism of fluorescence. All obtained compounds appeared to be non-toxic in a broad range of concentrations, during the in vitro experiments. Styrylquinolines maintained their fluorescent properties in biological systems, thus allowing for staining applications to use them. Their selective accumulation in the cellular organelles was also investigated, which indicated a preference for structures such as the mitochondria and the endoplasmic reticulum.

Author Contributions: Conceptualization R.M.; chemical synthesis B.C., M.K.; physical investigation B.C., A.S.; biological assays K.M., A.M.-W.; Funding acquisition K.M., A.M.-W.; original draft preparation B.C., K.M., A.M.W.; text review and editing R.M.; project administration R.M. All authors have read and agreed to the published version of the manuscript.

Funding: The authors wish to thank the National Center for Science grants: 2014/13/D/NZ7/00322 (A.M.W.) and 2016/23/N/NZ7/00351 (K.M.).

Acknowledgments: The Gaussian 09 calculations were performed in the Wrocław Centre for Networking and Supercomputing, WCSS, Wrocław, Poland: <http://www.wcss.wroc.pl>, under calculation Grant No. 18.

Conflicts of Interest: The authors declare no conflict of interest.

References

1. Mikata, Y.; Wakamatsu, M.; Kawamura, A.; Yamanaka, N.; Yano, S.; Odani, A.; Morihiro, K.; Tamotsu, S. Methoxy-Substituted TQEN Family of Fluorescent Zinc Sensors. *Inorg. Chem.* **2006**, *45*, 9262–9268. [[CrossRef](#)] [[PubMed](#)]
2. Musiol, R.; Serda, M.; Hensel-Bielowka, S.; Polanski, J. Quinoline-Based Antifungals. *Curr. Med. Chem.* **2010**, *17*, 1960–1973. [[CrossRef](#)]
3. Musiol, R. Quinoline-based HIV integrase inhibitors. *Curr. Pharm. Des.* **2013**, *19*, 1835–1849. [[CrossRef](#)] [[PubMed](#)]
4. Afzal, O.; Kumar, S.; Haider, R.; Ali, R.; Kumar, R.; Jaggi, M.; Bawa, S. A review on anticancer potential of bioactive heterocycle quinoline. *Eur. J. Med. Chem.* **2015**, *97*, 871–910. [[CrossRef](#)]
5. Polanski, J.; Kurczyk, A.; Bak, A.; Musiol, R. Privileged structures—Dream or reality: Preferential organization of azanaphthalene scaffold. *Curr. Med. Chem.* **2012**, *19*, 1921–1945. [[CrossRef](#)] [[PubMed](#)]
6. Podeszwa, B.; Niedbala, H.; Polanski, J.; Musiol, R.; Tabak, D.; Finster, J.; Serafin, K.; Milczarek, M.; Wietrzyk, J.; Boryczka, S.; et al. Investigating the antiproliferative activity of quinoline-5,8-diones and styrylquinolinecarboxylic acids on tumor cell lines. *Bioorg. Med. Chem. Lett.* **2007**, *17*, 6138–6141. [[CrossRef](#)]
7. Musiol, R.; Tabak, D.; Niedbala, H.; Podeszwa, B.; Jampilek, J.; Král'ová, K.; Dohnal, J.; Finster, J.; Mencil, A.; Polanski, J. Investigating biological activity spectrum for novel quinoline analogues 2: Hydroxyquinolinecarboxamides with photosynthesis-inhibiting activity. *Bioorganic Med. Chem.* **2008**, *16*, 4490–4499. [[CrossRef](#)]

8. Jampilek, J.; Musiol, R.; Finster, J.; Peško, M.; Carroll, J.; Králová, K.; Vejsová, M.; O'Mahony, J.; Coffey, A.; Dohnal, J.; et al. Investigating Biological Activity Spectrum for Novel Styrylquinazoline Analogues. *Molecules* **2009**, *14*, 4246–4265. [[CrossRef](#)]
9. Cieslik, W.; Musiol, R.; Nycz, J.E.; Jampilek, J.; Vejsová, M.; Wolff, M.; Machura, B.; Polanski, J. Contribution to investigation of antimicrobial activity of styrylquinolines. *Bioorganic Med. Chem.* **2012**, *20*, 6960–6968. [[CrossRef](#)]
10. Mrozek-Wilczkiewicz, A.; Spaczynska, E.; Malarz, K.; Ciešlik, W.; Rams-Baron, M.; Krystof, V.; Musiol, R. Design, Synthesis and In Vitro Activity of Anticancer Styrylquinolines. The p53 Independent Mechanism of Action. *PLoS ONE* **2015**, *10*, e0142678. [[CrossRef](#)]
11. Rams-Baron, M.; Dulski, M.; Mrozek-Wilczkiewicz, A.; Korzec, M.; Ciešlik, W.; Spaczynska, E.; Bartczak, P.; Ratuszna, A.; Polanski, J.; Musiol, R. Synthesis of New Styrylquinoline Cellular Dyes, Fluorescent Properties, Cellular Localization and Cytotoxic Behavior. *PLoS ONE* **2015**, *10*, e0131210. [[CrossRef](#)]
12. Zipper, H.; Brunner, H.; Bernhagen, J.; Vitzthum, F. Investigations on DNA intercalation and surface binding by SYBR Green I, its structure determination and methodological implications. *Nucleic Acids Res.* **2004**, *32*, e103. [[CrossRef](#)] [[PubMed](#)]
13. Carlsson, C.; Larsson, A.; Jönsson, M.; Albinsson, B.; Nordén, B. Optical and Photophysical Properties of the Oxazole Yellow DNA Probes YO and YOYO. *J. Phys. Chem.* **1994**, *98*, 10313–10321. [[CrossRef](#)]
14. Singer, V.L.; Jones, L.J.; Yue, S.T.; Haugland, R.P. Characterization of PicoGreen Reagent and Development of a Fluorescence-Based Solution Assay for Double-Stranded DNA Quantitation. *Anal. Biochem.* **1997**, *249*, 228–238. [[CrossRef](#)] [[PubMed](#)]
15. Hirons, G.T.; Fawcett, J.J.; Crissman, H.A. TOTO and YOYO: New very bright fluorochromes for DNA content analyses by flow cytometry. *Cytometry* **1994**, *15*, 129–140. [[CrossRef](#)]
16. Staderini, M.; Aulić, S.; Bartolini, M.; Tran, H.N.A.; González-Ruiz, V.; Pérez, D.I.; Cabezas, N.; Martínez, A.; Martín, M.A.; Andrisano, V.; et al. A Fluorescent Styrylquinoline with Combined Therapeutic and Diagnostic Activities against Alzheimer's and Prion Diseases. *ACS Med. Chem. Lett.* **2013**, *4*, 225–229. [[CrossRef](#)]
17. Dhanapal, R.; Perumal, P.T.; Damodiran, M.; Ramprasath, C.; Mathivanan, N. Synthesis of quinoline derivatives for fluorescent imaging certain bacteria. *Bioorganic Med. Chem. Lett.* **2012**, *22*, 6494–6497. [[CrossRef](#)]
18. Meng, X.; Wang, S.; Kang, X. Quinoline-Based Fluorescence Sensors. In *Molecular Photochemistry—Various Aspects*; IntechOpen: London, UK, 2012. [[CrossRef](#)]
19. Lee, H.G.; Lee, J.H.; Jang, S.P.; Hwang, I.H.; Kim, S.-J.; Kim, Y.; Kim, C.; Harrison, R.G. Zinc selective chemosensors based on the flexible dipicolylamine and quinoline. *Inorganica Chim. Acta* **2013**, *394*, 542–551. [[CrossRef](#)]
20. McQuade, L.E.; Lippard, S.J. Cell-Trappable Quinoline-Derivatized Fluoresceins for Selective and Reversible Biological Zn(II) Detection. *Inorg. Chem.* **2010**, *49*, 9535–9545. [[CrossRef](#)]
21. Kim, H.; Kang, J.; Kim, K.B.; Song, E.J.; Kim, C. A highly selective quinoline-based fluorescent sensor for Zn(II). *Spectrochim. Acta Part A Mol. Biomol. Spectrosc.* **2014**, *118*, 883–887. [[CrossRef](#)]
22. Xie, G.; Xi, P.; Wang, X.; Zhao, X.; Huang, L.; Chen, F.; Wu, Y.; Yao, X.; Zeng, Z. A Highly Zinc(II)-Selective Fluorescent Sensor Based on 8-Aminoquinoline and Its Application in Biological Imaging. *Eur. J. Inorg. Chem.* **2011**, *2011*, 2927–2931. [[CrossRef](#)]
23. Mahanand, D.; Houck, J.C. Fluorometric Determination of Zinc in Biologic Fluids. *Clin. Chem.* **1968**, *14*, 6–11. [[CrossRef](#)]
24. Cinar, R.; Nordmann, J.; Dirksen, E.; Müller, T.J.J. Domino synthesis of protochromic “ON–OFF–ON” luminescent 2-styryl quinolines. *Org. Biomol. Chem.* **2013**, *11*, 2597. [[CrossRef](#)] [[PubMed](#)]
25. Malathi, M.; Mohan, P.S.; Butcher, R.J.; Venil, C.K. Benzimidazole quinoline derivatives—An effective green fluorescent dye for bacterial imaging. *Can. J. Chem.* **2009**, *87*, 1692–1703. [[CrossRef](#)]
26. Yang, G.; Li, S.; Wang, S.; Hu, R.; Feng, J.; Li, Y.; Qian, Y. Novel fluorescent probes based on intramolecular charge- and proton-transfer compounds. *Pure Appl. Chem.* **2013**, *85*, 1465–1478. [[CrossRef](#)]
27. Fernández-Suárez, M.; Ting, A.Y.; Fern, M. Fluorescent probes for super-resolution imaging in living cells. *Nat. Rev. Mol. Cell Biol.* **2008**, *9*, 929–943. [[CrossRef](#)] [[PubMed](#)]
28. Hell, S. Toward fluorescence nanoscopy. *Nat. Biotechnol.* **2003**, *21*, 1347–1355. [[CrossRef](#)]
29. Sednev, M.V.; Belov, V.N.; Hell, S.W. Fluorescent dyes with large Stokes shifts for super-resolution optical microscopy of biological objects: A review. *Methods Appl. Fluoresc.* **2015**, *3*, 42004. [[CrossRef](#)]

30. Santana-Calvo, C.; Romero, F.; López-González, I.; Nishigaki, T. Robust evaluation of intermolecular FRET using a large Stokes shift fluorophore as a donor. *BioTechniques* **2018**, *65*, 211–218. [[CrossRef](#)]
31. Li, Y.; Liu, T.; Liu, H.; Tian, M.-Z.; Li, Y. Self-Assembly of Intramolecular Charge-Transfer Compounds into Functional Molecular Systems. *Accounts Chem. Res.* **2014**, *47*, 1186–1198. [[CrossRef](#)]
32. Suresh, M.; Kar, P.; Das, A. Intramolecular Charge Transfer aromatic amines and their application towards molecular logic gate. *Inorganica Chim. Acta* **2010**, *363*, 2881–2885. [[CrossRef](#)]
33. Xu, L.; Zhao, Y.; Long, G.; Wang, Y.; Zhao, J.; Li, D.; Li, J.; Ganguly, R.; Li, Y.; Sun, H.; et al. Synthesis, structure, physical properties and OLED application of pyrazine–triphenylamine fused conjugated compounds. *RSC Adv.* **2015**, *5*, 63080–63086. [[CrossRef](#)]
34. Das, R.; Guha, D.; Mitra, S.; Kar, S.; Lahiri, S.; Mukherjee, S. Intramolecular Charge Transfer as Probing Reaction: Fluorescence Monitoring of Protein–Surfactant Interaction. *J. Phys. Chem. A* **1997**, *101*, 4042–4047. [[CrossRef](#)]
35. Kumar, C.V.; Tolosa, L.M. New charge-transfer probe for solvent polarity; fluorescent hydrogen-bonding switch. *J. Chem. Soc. Chem. Commun.* **1993**, 722. [[CrossRef](#)]
36. Prakash, A.; Adhikari, D. Application of Schiff bases and their metal complexes-A review. *Int. J. Chem. Tech. Res.* **2011**, *3*, 1891–1896.
37. Kajal, A.; Bala, S.; Kamboj, S.; Sharma, N.; Saini, V. Schiff Bases: A Versatile Pharmacophore. *J. Catal.* **2013**, *2013*, 1–14. [[CrossRef](#)]
38. Brodowska, K.; Lodyga-Chruscinska, E. ChemInform Abstract: Schiff Bases - Interesting Range of Applications in Various Fields of Science. *Cheminform* **2015**, *46*, 129–134. [[CrossRef](#)]
39. Qin, J.-C.; Li, T.-R.; Wang, B.-D.; Yang, Z.-Y.; Fan, L. A sensor for selective detection of Al³⁺ based on quinoline Schiff-base in aqueous media. *Synth. Met.* **2014**, *195*, 141–146. [[CrossRef](#)]
40. Halder, S.; Dey, S.; Roy, P. A quinoline based Schiff-base compound as pH sensor. *RSC Adv.* **2015**, *5*, 54873–54881. [[CrossRef](#)]
41. Mason, W.T. (Ed.) *Fluorescent and Luminescent Probes for Biological Activity*, 2nd ed.; Academic Press: London, UK, 1999.
42. Menter, J.M. Temperature dependence of collagen fluorescence. *Photochem. Photobiol. Sci.* **2006**, *5*, 403. [[CrossRef](#)]
43. Ghisaidoobe, A.B.T.; Chung, S.J. Intrinsic Tryptophan Fluorescence in the Detection and Analysis of Proteins: A Focus on Förster Resonance Energy Transfer Techniques. *Int. J. Mol. Sci.* **2014**, *15*, 22518–22538. [[CrossRef](#)]
44. Georgakoudi, I.; Jacobson, B.C.; Müller, M.G.; Sheets, E.E.; Badizadegan, K.; Carr-Locke, D.L.; Crum, C.; Boone, C.W.; Dasari, R.R.; Van Dam, J.; et al. NAD(P)H and collagen as in vivo quantitative fluorescent biomarkers of epithelial precancerous changes. *Cancer Res.* **2002**, *62*, 682–687. [[PubMed](#)]
45. Lakowicz, J.R. *Principles of Fluorescence Spectroscopy*; Springer Science and Business Media LLC: Amsterdam, The Netherlands, 2006.
46. Valeur, B. *Molecular Fluorescence: Principles and Applications*; Wiley-VCH: Berlin, Germany, 2001.
47. Thiagarajan, V.; Selvaraju, C.; Malar, E.J.P.; Ramamurthy, P. A Novel Fluorophore with Dual Fluorescence: Local Excited State and Photoinduced Electron-Transfer-Promoted Charge-Transfer State. *ChemPhysChem* **2004**, *5*, 1200–1209. [[CrossRef](#)] [[PubMed](#)]
48. Czaplińska, B.; Malarz, K.; Mrozek-Wilczkiewicz, A.; Musiol, R. Acid selective pro-dye for cellular compartments. *Sci. Rep.* **2019**, *9*, 15304. [[CrossRef](#)] [[PubMed](#)]
49. Lippert, E. Dipolmoment und Elektronenstruktur von angeregten Molekülen. *Zeitschrift für Naturforschung A* **1955**, *10*, 541–545. [[CrossRef](#)]
50. Mataga, N.; Kaifu, Y.; Koizumi, M. The solvent effect on fluorescence spectrum – change of solute-solvent interaction during the lifetime of excited solute molecule. *Bull. Chem. Soc. Jpn.* **1955**, *28*, 690–691. [[CrossRef](#)]
51. Gong, Y.; Guo, X.; Wang, S.; Su, H.; Xia, A.; He, Q.; Bai, F. Photophysical Properties of Photoactive Molecules with Conjugated Push–Pull Structures. *J. Phys. Chem. A* **2007**, *111*, 5806–5812. [[CrossRef](#)]
52. Jia, M.; Ma, X.; Yan, L.; Wang, H.; Guo, Q.; Wang, X.; Wang, Y.; Zhan, X.; Xia, A. Photophysical Properties of Intramolecular Charge Transfer in Two Newly Synthesized Tribranched Donor– π –Acceptor Chromophores. *J. Phys. Chem. A* **2010**, *114*, 7345–7352. [[CrossRef](#)]
53. Colston, J.; Horobin, R.W.; Rashid-Doubell, F.; Padiani, J.; Johal, K.K. Why fluorescent probes for endoplasmic reticulum are selective: An experimental and QSAR-modelling study. *Biotech. Histochem.* **2003**, *78*, 323–332. [[CrossRef](#)]

54. Frisch, M.J.; Trucks, G.W.; Schlegel, H.B.; Scuseria, G.E.; Robb, M.A.; Cheeseman, J.R.; Scalmani, G.; Barone, V.; Petersson, G.A.; Nakatsuji, H.; et al. *Gaussian 09, Revision E.01 2013*; Gaussian Inc.: Wallingford, CT, USA, 2013.
55. Stephens, P.J.; Devlin, F.J.; Chabalowski, C.F.; Frisch, M.J. Ab Initio Calculation of Vibrational Absorption and Circular Dichroism Spectra Using Density Functional Force Fields. *J. Phys. Chem.* **1994**, *98*, 11623–11627. [[CrossRef](#)]
56. Becke, A.D. Density-functional thermochemistry. III. The role of exact exchange. *J. Chem. Phys.* **1993**, *98*, 5648–5652. [[CrossRef](#)]
57. Lee, C.; Yang, W.; Parr, R.G. Development of the Colle-Salvetti correlation-energy formula into a functional of the electron density. *Phys. Rev. B* **1988**, *37*, 785–789. [[CrossRef](#)]
58. Yanai, T.; Tew, D.P.; Handy, N.C. A new hybrid exchange—Correlation functional using the Coulomb—Attenuating method (CAM—B3LYP). *Chem. Phys. Lett.* **2004**, *393*, 51–57. [[CrossRef](#)]
59. Cossi, M.; Barone, V.; Cammi, R.; Tomasi, J. Ab initio study of solvated molecules: A new implementation of the polarizable continuum model. *Chem. Phys. Lett.* **1996**, *255*, 327–335. [[CrossRef](#)]
60. Foresman, J.B.; Keith, T.A.; Wiberg, K.B.; Snoonian, J.; Frisch, M.J. Solvent Effects. Influence of Cavity Shape, Truncation of Electrostatics, and Electron Correlation on ab Initio Reaction Field Calculations. *J. Phys. Chem.* **1996**, *100*, 16098–16104. [[CrossRef](#)]
61. Tomasi, J.; Mennucci, B.; Cancès, E. The IEF version of the PCM solvation method: An overview of a new method addressed to study molecular solutes at the QM ab initio level. *J. Mol. Struct. THEOCHEM* **1999**, *464*, 211–226. [[CrossRef](#)]

Sample Availability: Samples of the compounds are available from the authors.



© 2020 by the authors. Licensee MDPI, Basel, Switzerland. This article is an open access article distributed under the terms and conditions of the Creative Commons Attribution (CC BY) license (<http://creativecommons.org/licenses/by/4.0/>).